Effect of the Particle Size of 316L Stainless Steel on the Corrosion Characteristics of the Steel Fabricated by Selective Laser Melting

Wei Chen[1], Guangfu Yin[1,*], Zhongbing Huang[1], Zai Feng[2]

[1] College of Materials Science and Engineering, Sichuan University, Chengdu, 610065, China
[2] Sichuan Hengchuang Bolian Technology Co., Ltd, Chengdu, 610044, China
[*]E-mail: nic0700@scu.edu.cn

The corrosion characteristics of 316L stainless steel (SS316L) fabricated by selective laser melting (SLM) in a 6.0 wt.% $FeCl_3$ solution was investigated in this study. To analyse the relationship between the corrosion factor and powder feedstock, three samples were made by SLM with three particle sizes, and their potentiodynamic polarization curve were measured using a CHI660E electrochemical working station in a 6.0 wt.% $FeCl_3$ solution at 25 °C. The microstructure was investigated by optical microscopy (OM) and scanning electron microscopy (SEM). Corrosion products analyses were performed using an X-ray energy dispersion spectroscopy (EDS) detection system. The results showed that the SLM samples prepared with fine powder possessed the best surface quality with a much lower porosity and without un-melted powder particles. Compared with the SLM samples from the coarse powder and raw powder, the SLM samples from fine powder exhibited a higher corrosion potential (E_{corr}) by 18.94 %, 28.09 % and 67.33 % at the XY-plane, the XZ-plane and the YZ-plane, respectively. However, the corrosion current density (i_{corr}) at the three cross-sections of the SLM sample from fine powder was not lower than that of the other two samples. The weight loss of the SLM sample from fine powder was the highest. These results indicated that the corrosion tendency of the SLM sample from the fine powder was the lowest, but its corrosion rate was the fastest.

1. INTRODUCTION

An additive manufacturing (AM) production technique, commonly referred to as 3D printing, is a combination of computer-aided design (CAD), material processing and forming technology. Using

this technique, it is possible to manufacture high-accuracy and more complex structural parts that could not be previously produced by traditional manufacturing methods. AM technologies include laminated object manufacturing (LOM) [1], directed energy deposition (DED) [2], stereo lithography appearance (SLA) [3], selective laser sintering (SLS) [4], selective laser melting (SLM) [5], electron beam melting (EBM) [6] and binder jet 3D printing (BJ3DP) [7]. SLM has been one of the most used powder bed AM processes developed for rapid prototyping with metal powders, which can be used to produce metal parts with almost complete density, excellent mechanical properties, high dimensional accuracy, and a high material utilization ratio. A great deal of studies has been performed to establish the relationship among the process, microstructure, defects and mechanical performance for stainless steel [8], aluminium [9], nickel [10], pure tantalum and titanium alloys [11,12]. SLM has attracted the interest of a large number of researchers' in multiple domains such as the aerospace [13], nuclear and biomedical industries [11,14].

316L stainless steel (SS316L) is a type of austenitic stainless steel with high corrosion resistance and could be utilized in the medicine and food industries [15-17]. The corrosion resistance of SS316L produced by SLM has been researched. It is generally known that the corrosion resistance of stainless steel is mainly determined by its chemical composition, microstructure and porous defects. These factors are also controlled by the initial SLM processing parameters such as laser power, scanning speed, hatch distance, layer thickness and beam spot diameter. The corrosion characteristics of as-cast and sintered SS316L samples in sulphuric acid and phosphoric acid solution were studied [18]. It was found that compared to cast samples, the sintered samples exhibited a lower corrosion resistance in both solutions due to the presence of residual pores in the microstructure. The effect of the porosity on the corrosion behaviour of hot-pressed stainless steel (HPSS) in sulphuric acid was investigated [19]. The results showed that the porosity of HPSS was the major factor affecting its corrosion resistance. The high porosity led to a low corrosion resistance. It was shown that the primary mechanism that affected the corrosion resistance of HPSS in a H_2SO_4 solution was the evolution of the hydrogen concentration cell produced by the electrolysis stall in the communication open cell. Thus, the exposed cell surface during communication served as an active anode, and the surface of the engineering sample acted as an active cathode. The relationship between surface quality and corrosion resistance of the SLM SS316L sample was inspected [16]. The results indicate that high surface quality could enhance the corrosion resistance of the SS316L parts manufactured via SLM. The corrosion behaviour of grade SS316L fabricated using casting, hot isostatic pressing (HIP), SLM and SLM + HIP in H_2SO_4 solution was examined [17]. The electrochemical results showed that the manufacturing method had a significant effect on the corrosion resistance of SS316L parts. The effect of the powder size distribution on the sintering kinetics along with empirical models for solid-state and supersolidus liquid phase sintering (SLPS) of Inconel 718 parts fabricated by BJ3DP was discussed [20]. The results indicated that the powder size distribution affected the properties of the 3D printed parts.

Various experiments have been conducted to research the relationship between the processing parameters and properties of SS316L produced by SLM. However, the role of powder size on the corrosion characteristics of SLM SS316L is lacking. In this study, SS316L samples prepared by SLM

with three particle sizes were used to investigate the relationship between the particle size and corrosion characteristics in a 6.0 wt.% $FeCl_3$ solution.

2. EXPERIMENTAL PROCEDURE

2.1. SS316L powder

The SS316L spherical powder was prepared by a gas atomization process with the following parameters: an atomization temperature of 1550-1600 °C, a liquid-metal flow velocity of 10 kg/min, and an inlet nitrogen gas pressure of 6.0 MPa. Mesh sieving and cyclone separation were used to select the three kinds of SS316L powders with a median particle size (d_{50}) of 8.29 μm (fine powder), 20.31 μm (coarse powder) and 14.63 μm (raw powder) with a composition of Cr 17.42 wt.%, Ni 11.61 wt.%, Mo 2.27 wt.%, Mn 1.49 wt.%, Si 0.75 wt.%, C 0.019 wt.%, P 0.008 wt.%, S 0.003 wt.%, O 0.005 wt.% and the balance Fe for SLM processing. The microstructure of the three sizes of the SS316L powders was presented in Figure 1, which shows a highly spherical shape suitable for the SLM process.
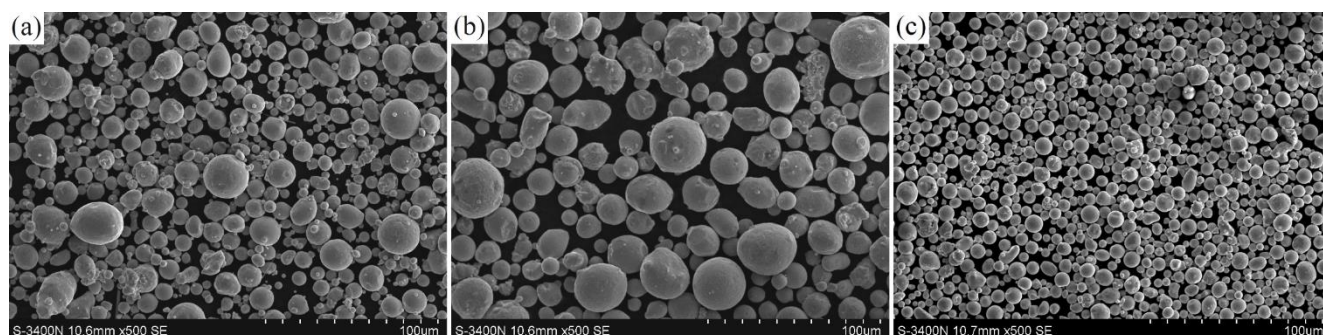
Figure 1. SEM morphologies of three SS316L raw powder (a), coarse powder (b) and fine powder (c).

2.2. Selective laser melting (SLM)
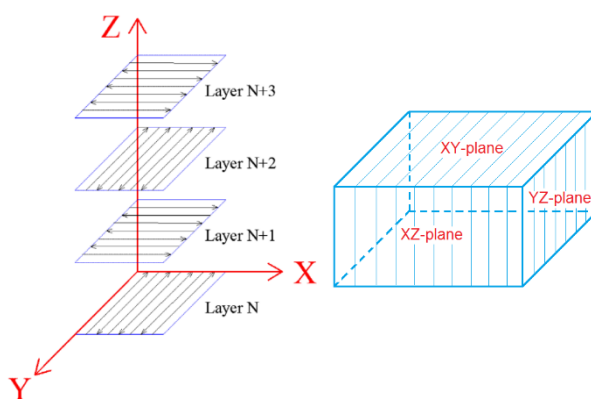
Figure 2. Schematic diagram of laser scanning path strategy.

The metallic parts were manufactured using the SLM process by the AFS-M120 (Longyuan AFS Co. Beijing, China). The processing parameters were as follows: maximum laser power of 500 W, laser spot diameter of 70 μm, hatch distance of 60 μm, scanning speed of 2000 mm/s and layer thickness of 30 μm. The schematic diagram of laser scanning path strategy is shown in Figure 2. The XY-plane was the scanning direction, and the YZ-plane and XZ-plane were the building directions.

2.3. Electrochemical tests

The potentiodynamic polarization curves were measured using a CHI660E electrochemical working station at 25 °C in a 6.0 wt.% $FeCl_3$ solution. The test cell included a saturated calomel electrode as the reference electrode, a platinum counter electrode, and the SS316L SLM sample as the working electrode. The working electrode was embedded in epoxy resin with only an exposed area of 0.25 cm^2 that remained for testing. The polarization curves were swept at a scan rate of 1 mV/s from an initial potential of -1.0 V to a final potential of 1.2 V [21] and started after a 30 min immersion of the samples in a 6.0 wt.% $FeCl_3$ solution. Three independent trials were conducted under the same conditions.

2.4. Immersion corrosion experiment

In the immersion corrosion tests, the square-shaped samples were polished using SiC paper from 320 grit down to 2000 grit. The samples were cleaned with ethanol and the initial weight as well as the dimensions of the samples was measured. The samples were then immersed in a 6.0 wt.% $FeCl_3$ solution. The samples were removed from the solution every 24 h, then washed with distilled water, dried in hot air and then weighed by an analytical balance (Zhuojing Co. Shanghai, China) with the smallest increment of 0.1 mg. The samples were then re-immersed in the $FeCl_3$ solution again for 24 h. The corrosion products were not deliberately removed at any intermediate stages but were removed only after the last analysis for microscopic investigations. Three independent trials were conducted under the same conditions after a time period of 1, 2, 3, …, 25 days.

2.5. Characterization

Metallographic specimens were cut from the SLM parts using an electric discharge wire, polished with a series of silicon carbide (SiC) sandpaper (320, 800, 1200 and 2000 grit) and ground with a diamond suspension from 5 μm down to 1 μm to achieve a mirror finish. An Olympus-PMG3 optical microscope was used to examine the microstructures of all samples, which were etched by a solution (10 ml HNO_3, 10 ml HCl and 50 ml H_2O) for 30 s at room temperature. A detailed microstructural analysis was performed using a TM-1000 scanning electron microscope (at low magnification) and a FEI Quanta FEG 250 scanning electron microscope (SEM) (at higher magnification) equipped with an X-ray energy dispersion spectroscopy (EDS) detection system, using a working distance of 15 mm and an acceleration voltage of 20 keV. The phase characterization of the

corrosion products was measured by X-ray diffraction (XRD, D8 Advance, Bruker, Germany) with Cu-K$_\alpha$ radiation with a wavelength of 1.5405 Å at 40 kV and 40 mA in the 2-theta range 0-90° at a scan rate of 0.05°/s.

3. RESULTS AND DISCUSSION

3.1. Potentiodynamic polarization curves

Figure 3 shows the potentiodynamic polarization curves of the three SS316L SLM samples. It could be seen that there was no passivation platform on the potentiodynamic polarization curves. Electrochemical parameters including the corrosion potential (E_{corr}), the corrosion current density (i_{corr}), the cathodic Tafel slope (b$_c$) and the anodic Tafel slope (b$_a$) were calculated by Tafel extrapolation from Figure 3, and the results are shown in Table 1. These parameters are normally used to represent the active dissolution of the materials in the form of E_{corr} and i_{corr} [22]. The E_{corr} of the SS316L SLM samples from coarse powder and raw powder at the XY-plane were 0.095 V and 0.096 V, at the XZ-plane were 0.089 V and 0.093 V, and at the YZ-plane were 0.101 V and 0.098 V, respectively. The E_{corr} of the SS316L SLM samples from fine powder was higher than that from coarse powder and raw powder at three planes. The E_{corr} of the SS316L SLM samples from coarse powder and raw powder was similar at the three planes. Additionally, the i_{corr} data indicated that the SS316L SLM fine powder YZ-plane sample exhibited the highest i_{corr} (approximately 38.68 µA/cm^2).
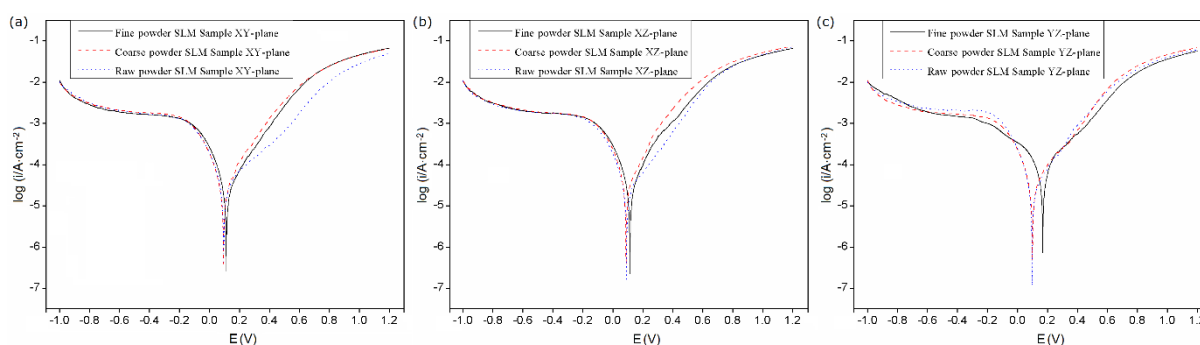
Figure 3. Polarization curves of the SS316L SLM samples' XY-Plane (a), XZ-Plane (b) and YZ-Plane (c) in a 6.0 wt.% FeCl$_3$ solution at 25 °C.

Based on electrochemical theory, E_{corr} evaluates the energy of a corrosion reaction and is a type of thermodynamics parameter. The higher the E_{corr} is, the greater the corrosion of the sample is. The i_{corr} evaluates the corrosion reaction rate and is a kind of kinetics parameter. The lower the i_{corr} is, the lower the corrosion reaction rate of the sample is [23]. Notably, compared with the SS316L SLM samples from the coarse powder and raw powder, the SS316L SLM samples from the fine powder exhibited a higher E_{corr} by 18.94%, 28.09% and 67.33% at XY-plane, XZ-plane and YZ-plane, respectively.

Table 1. Electrochemical parameters of three SS316L SLM samples in the 6.0 wt.% FeCl$_3$ solution at 25 °C.

Specimens		E_{corr} [V]	i_{corr} [μA/cm^2]	-b$_c$ [V/dec]	b$_a$ [V/dec]
Fine powder SLM Sample	XY-plane	0.113	17.58	0.07	0.11
	XZ-plane	0.114	19.27	0.08	0.10
	YZ-plane	0.169	38.68	0.10	0.09
Coarse powder SLM Sample	XY-plane	0.095	16.02	0.07	0.11
	XZ-plane	0.089	27.06	0.08	0.12
	YZ-plane	0.101	21.49	0.08	0.11
Raw powder SLM Sample	XY-plane	0.096	19.16	0.08	0.13
	XZ-plane	0.093	18.45	0.08	0.13
	YZ-plane	0.098	18.87	0.07	0.12
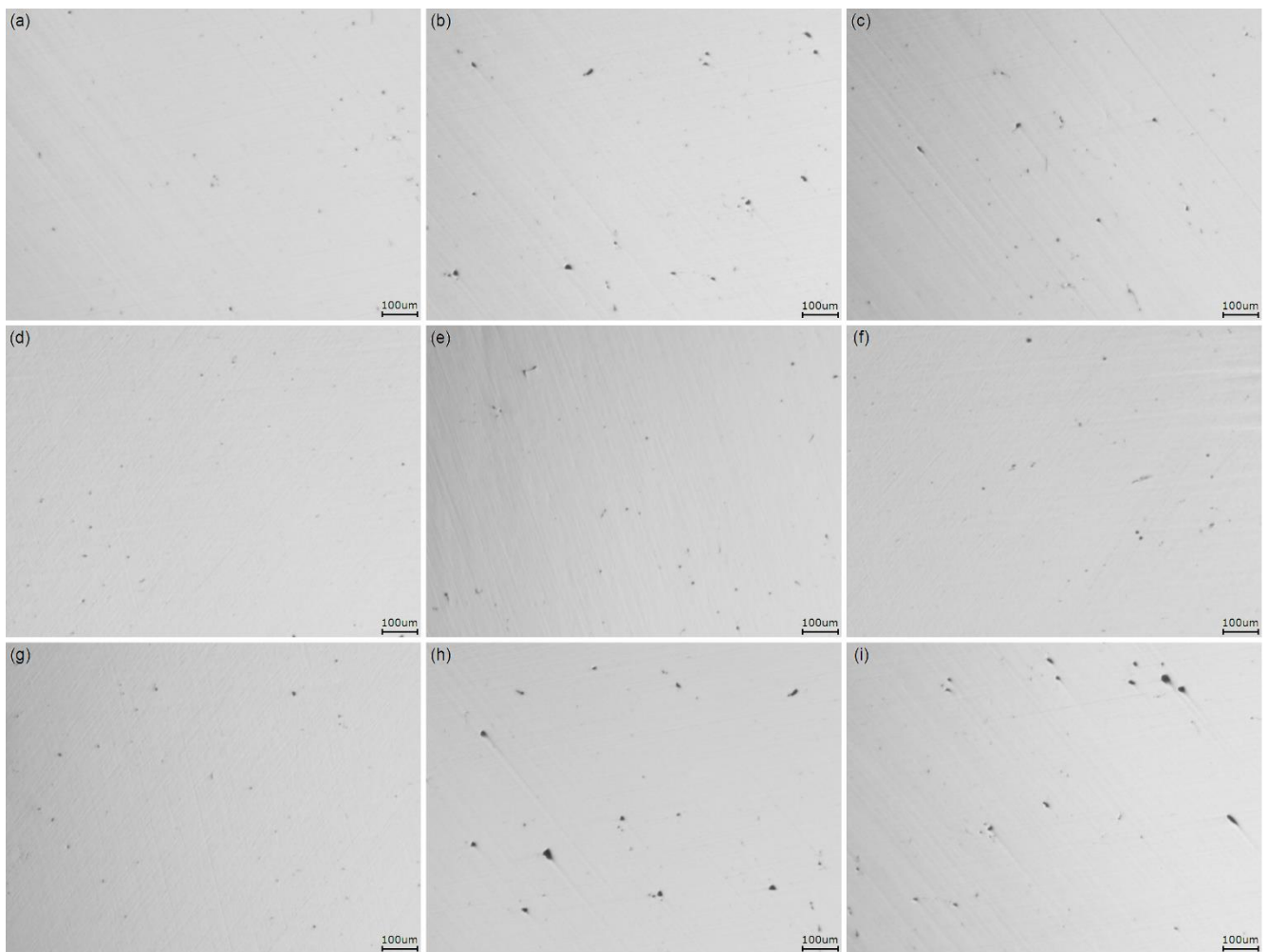
Figure 4. OM images of the fine powder XY plane (a), coarse powder XY plane (b), raw powder XY plane (c), fine powder YZ plane (d), coarse powder YZ plane (e), raw powder YZ plane (f), fine powder XZ plane (g), coarse powder XZ plane (h) and raw powder XZ plane (i).

However, the i_{corr} at the three cross-sections of the SLM fine powder sample was not lower than that of the other two samples. This result indicated that the corrosion tendency of the SS316L SLM sample from fine powder was the lowest, but its corrosion rate was the fast.
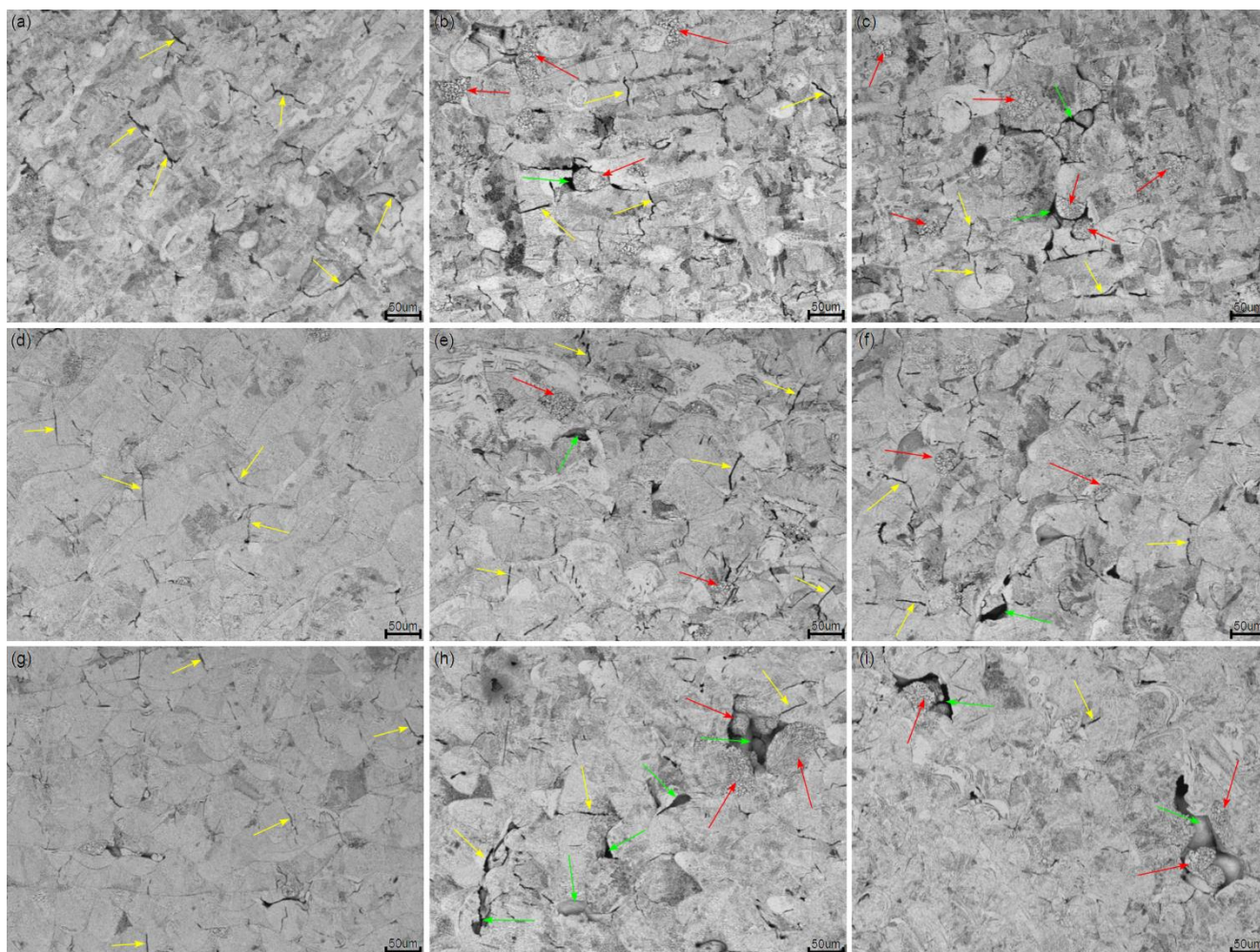
Figure 5. Microstructure of the fine powder XY plane (a), coarse powder XY plane (b), raw powder XY plane (c), fine powder YZ plane (d), coarse powder YZ plane (e), raw powder YZ plane (f), fine powder XZ plane (g), coarse powder XZ plane (h) and raw powder XZ plane (i).

As shown in Figure 4, the morphology of the SS316L SLM samples from different particle size distribution powders exhibited large differences. The SS316L SLM samples from fine powder had the best surface quality which was smoother with less porosity and defects, while the SS316L SLM samples from coarse powder and raw powder had the worst surface quality with vast porosity and defects.

Microcracks (yellow arrows), pores (green arrows) and un-melted powders (red arrows) were more distinct after the surface of the SLM samples were etched as shown in Figure 5. Compared with the coarse powder and raw powder samples, the surface of the fine powder sample possessed less pores and almost no un-melted powder, indicating that under the above conditions of the process parameters, the powder that could be directly affected by the laser in the SS316L SLM sample from the fine

powder was almost completely melted. The contents of the un-melted powders in the SS316L SLM samples from coarse powder and raw powder were the same.
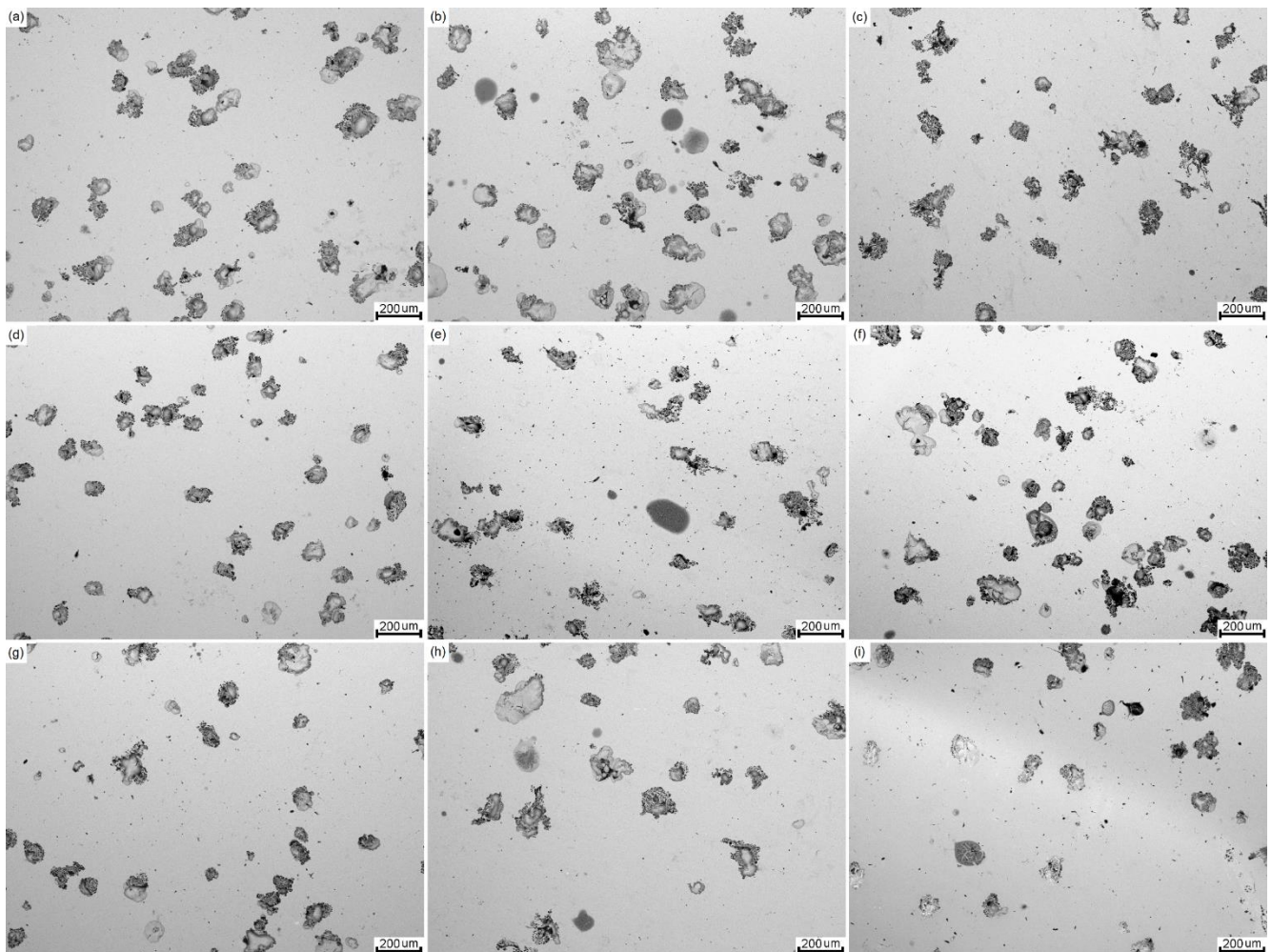
Figure 6. Low magnification of the SEM images of the SLM SS316L samples after anodic polarisation testing in a 6.0 wt.% FeCl$_3$ solution at 25 °C: fine powder XY plane (a), coarse powder XY plane (b), raw powder XY plane (c), fine powder YZ plane (d), coarse powder YZ plane (e), raw powder YZ plane (f), fine powder XZ plane (g), coarse powder XZ plane (h) and raw powder XZ plane (i).

The diameter of the un-melted powders was more than 30 μm as shown in Figure 5h and i. Additionally, there were large pores around the un-melted powder because the laser energy density was not high enough to melt the coarse powder completely, and un-melted powders were formed [24]. Simultaneously, the un-melted powder blocked the heat transfer of the laser beam, resulting in the formation of holes around the un-melted particles. The SS316L SLM samples from coarse powder and raw powder exhibited greater porosity. As a result, the corrosion was initiated first and easily formed a high corrosion potential. Once beginning, the corrosion progressed along the holes and pores, and the corrosion products assembled on the reaction zone hindering the ongoing reaction. Hence, the i_{corr} of the SLM samples from the coarse powder and raw powder at some planes were lower than the SLM

samples from the fine powder. The corrosion could only take place in the holes, pores and microcracks whose potential were high enough [19]. At the same time, the corrosion products dissolved in solution quickly [25].

Figure 6 shows the low magnification of the SEM images of the nine SLM SS316L samples after anodic polarisation testing in a 6.0 wt.% $FeCl_3$ solution at 25 °C. It could be seen that the corrosion morphology of the nine SLM SS316L samples was similar and the surface of the samples contained a large number of corrosion holes, which is typical pitting corrosion after this type of polarisation test in a 6.0 wt.% $FeCl_3$ solution. From Figure 6, the radius of most pits exceeded 50 μm. SS316L was particularly sensitive to pitting corrosion in the presence of chloride ions [26]. The Cr content of SS316L was high, and a passivation film could be formed in the 6.0 wt.% $FeCl_3$ solution. However, the chloride ion radius was very small, and it was easy to penetrate the passivation film, resulting in pitting corrosion, which limited the continuation of the passivation zone [27,28].

Chemical composition of different regions analysized by EDS

wt.%

Element	Fe	Cr	Ni	Mo	Mn	Si	C
316L	66.37	17.32	11.61	2.27	1.49	0.75	0.019
Area 1	67.65	20.24	6.03	0.60	5.24	0.09	0.14
Area 2	62.41	25.51	3.01	0.30	7.28	0.40	1.08
Area 3	71.06	15.16	10.64	1.12	1.72	0.30	0.00
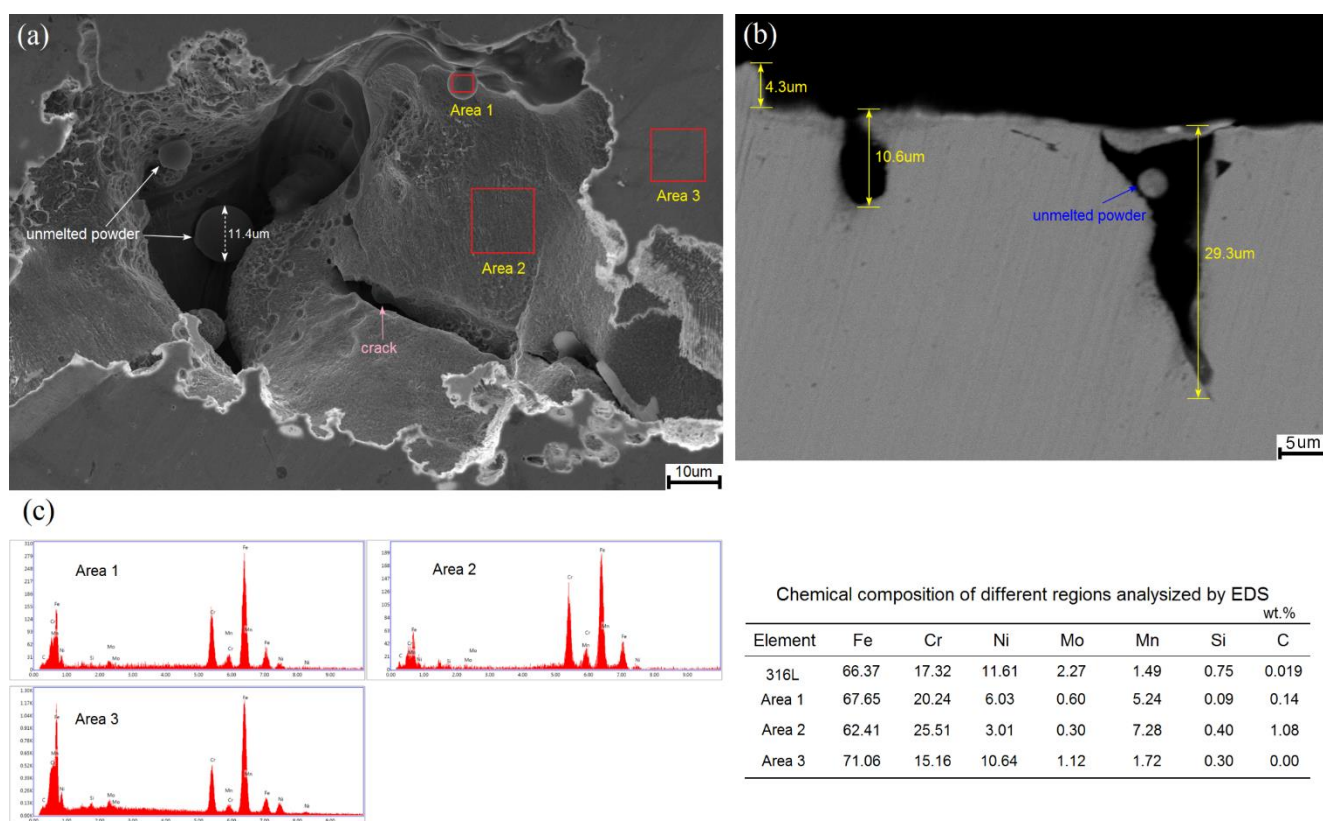
Figure 7. Higher magnification of the SEM images of the surface (a) and cross-section (b) of the SS316L SLM sample after anodic polarisation testing in a 6.0 wt.% $FeCl_3$ solution at 25 °C and an EDS analysis of selected areas on the surface (c).

Figure 7 shows the higher magnification of the SEM image and EDS analysis for different regions of the SS316L SLM samples after anodic polarisation testing in a 6.0 wt.% $FeCl_3$ solution at 25 °C. The presence of un-melted powder and cracks could be found in the corrosion pores [29], and large voids could clearly be seen around the un-melted powders, indicating that the un-melted powder has an excellent corrosion resistance in the 6.0 wt.% $FeCl_3$ solution. Due to the difference of the

microstructure between the un-melted powder and the re-melted area, microcells were easily formed, and the re-melted areas were more susceptible to corrosion in the 6.0 wt.% $FeCl_3$ solution, in which Fe^{3+} had stronger oxidizing properties. Moreover, sample corrosion was more likely to occur within the grain and micro cracks, which might be attributed to the larger specific surface area of the primary cracks and pore sites [30]. Therefore, a greater number of micro cracks, un-melted powders and pores inside the sample led to a stronger corrosion tendency of the samples in the $FeCl_3$ solution. Area 1 was located in the un-melted powder, area 2 was located at the corrosion surface, and area 3 was taken from the substrate of the SS316L SLM sample. Obviously, in comparison to the SS316L components, the Ni, Mo and Si contents in areas 1 and 2 evidently decreased, but the Cr and Mn contents increased remarkably. The contents of Ni and Mo in area 2 were significantly lower than those in areas 1 and 2, while the contents of Cr, Mn and C were significantly higher than those in areas 1 and 2. The Fe contents in areas 1, 2 and 3 were similar to those of the initial 316L state. It could be considered that the effect of Cr and Mn seemed to inhibit the activity of Fe, Mo and Ni intermediates and formed a barrier against pitting corrosion [31,32]. The cross-sectional SEM image of the SLM sample from the fine powder following corrosion testing in a 6.0 wt.% $FeCl_3$ solution is shown in Figure 7b. The depth of the crack propagation was up to 29.3 μm, and fine spherical powder with particle diameters less than 5 μm inside the crack was observed.

3.2. Weight loss tests after immersion corrosion experiment

Figure 8 presents the relationship between the weight loss and immersion time (in days) of the SS316L SLM samples from the fine powder, coarse powder, and raw powder in a 6.0 wt.% $FeCl_3$ solution at 25 °C. Obviously, the three curves showed a similar trend. With an increase in the immersion time, the weight loss rate increased [33]. However, the rate of growth slowed down over time. The results showed a weight loss of 71.64 ± 1.36 mg/cm^2, 69.28 ± 1.41 mg/cm^2, and 66.70 ± 1.32 mg/cm^2 for the SLM samples from fine powder, coarse powder, and raw powder, respectively, after 25 days of immersion. These results indicated that the increase in the weight loss of the SLM samples from fine powder was the fastest, while that of the SLM samples from raw powder was the slowest in the 6.0 wt.% $FeCl_3$ solution. The weight loss curves were nonlinear for all the SLM samples, i.e., during the first 5 days, the corrosion rate was very high. With an increase in the immersion time, the corrosion rate decreased gradually. This phenomenon could be attributed to the destruction of the passivation film by Cl$^-$ in the $FeCl_3$ solution, which subsequently attacked the substrate of SS316L SLM sample [34,35]. After immersion in the corresponding test solution for 5 days, the weight loss rate began to decrease gradually within a small range [33], which meant that the corrosion product layer formed on the surface of the metal electrolyte as a barrier and reduced the weight loss rate of the alloy samples. In addition to the above generality, the weight loss of the fine powder sample was significantly higher than that of the coarse powder sample and the raw powder sample at each test stage (shown in Figure 8). The results confirmed that the fine powder samples were more susceptible to corrosion than the SS316L SLM samples from the coarse powder and raw powder.
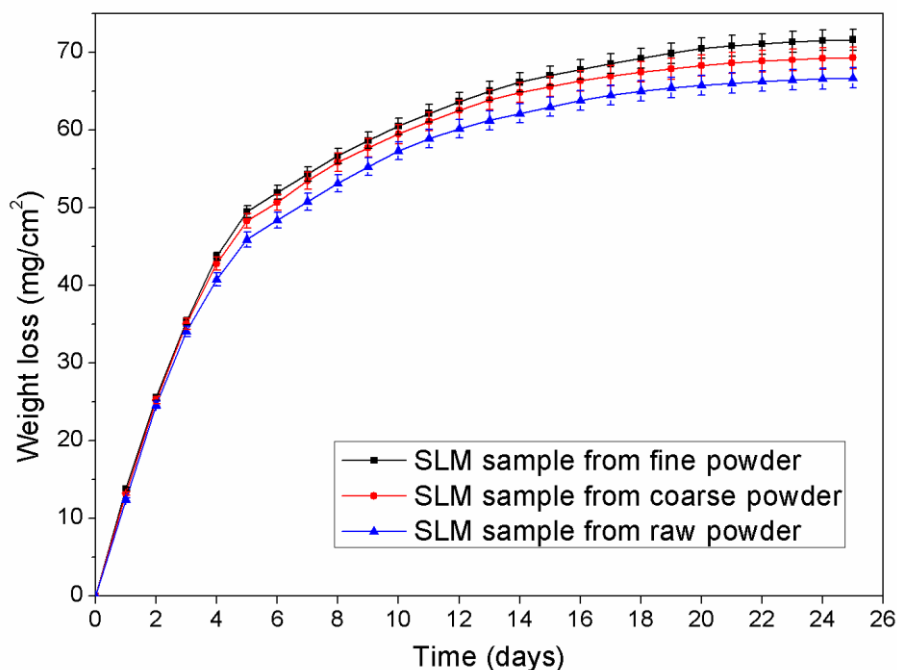
Figure 8. Weight loss plots for the SS316L SLM samples from fine powder, coarse powder and raw powder as a function of time in a 6.0 wt.% $FeCl_3$ solution at 25 °C.

Figure 9 displays the corrosion morphology of the surfaces of the SS316L SLM samples from the fine powder and coarse powder after immersion into a 6.0 wt.% $FeCl_3$ solution at 25 °C for 25 days. As shown in Figure 9a, the surface of fine powder sample that had indeed undergone severe pitting attacks and a typical pitting hole with diameter of 8 μm could be observed. Notably, the higher magnification SEM images in Figure 9b and c show that the corroded columnar grains, which had two kinds of structures, namely, one is similar to a vertical-bamboo structure (Figure 9b) and the other is similar to a flat-bamboo structure (Figure 9c), were completely consistent with the revealed structure of columnar grains. These results are in agreement with the mechanism interpreted by Chen [33]. However, the bamboo structure was more suitable than the peanut shell structure to explain the corrosion morphology of this paper because the structure of corroded columnar grains was straighter and smoother. On the surface of the fine powder sample, the corrosion products could be seen to fall off (Figure 9a-c), while the coarse powder sample had gathered a thick layer of corrosion products and some microcracks had been filled with corrosion products to prevent them from being further corroded (Figure 9d).
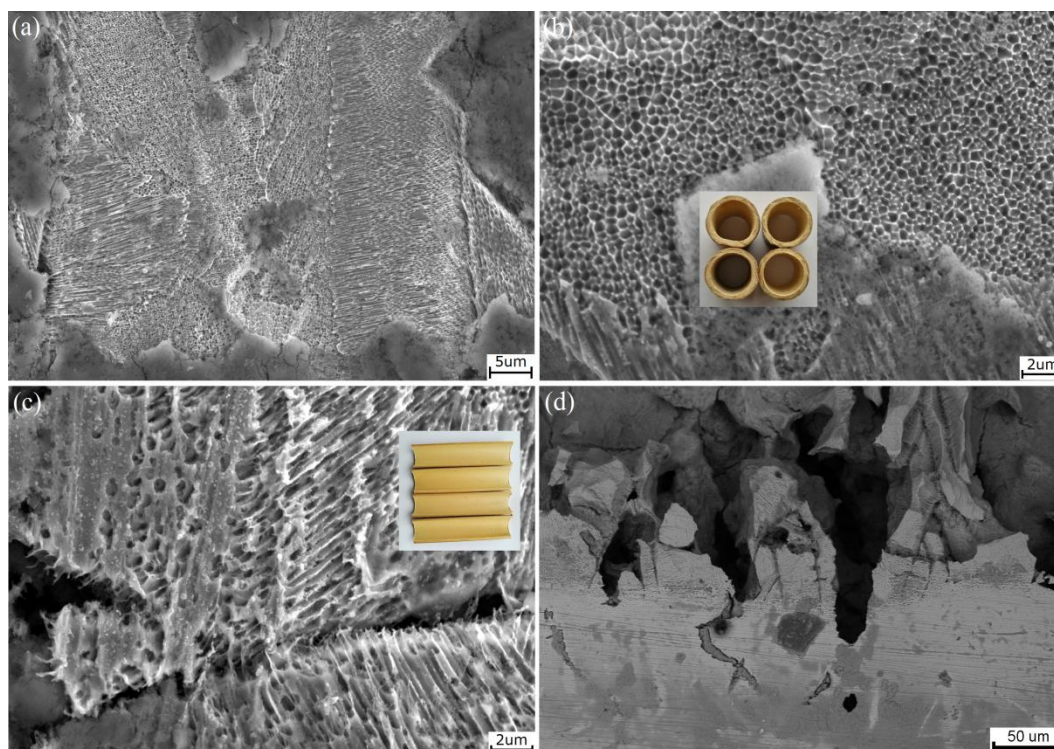
Figure 9. SEM images of the XY-plane (a), vertical bamboo structure (b), flat bamboo structure (c) of the SS316L SLM sample from fine powder and the XZ-plane (d) of the SS316L SLM sample from coarse powder after an immersion corrosion experiment in a 6.0 wt.% FeCl$_3$ solution at 25 °C for 25 days.

Chemical composition of different regions analysized by EDS

| | | | | | | | | | wt.% |
Element	Fe	Cr	Ni	Mo	Mn	Si	C	Cl	O
316L	66.37	17.32	11.61	2.27	1.49	0.75	0.019	/	/
Area 1	51.22	5.16	7.60	4.84	0.78	0.25	4.74	0.21	25.20
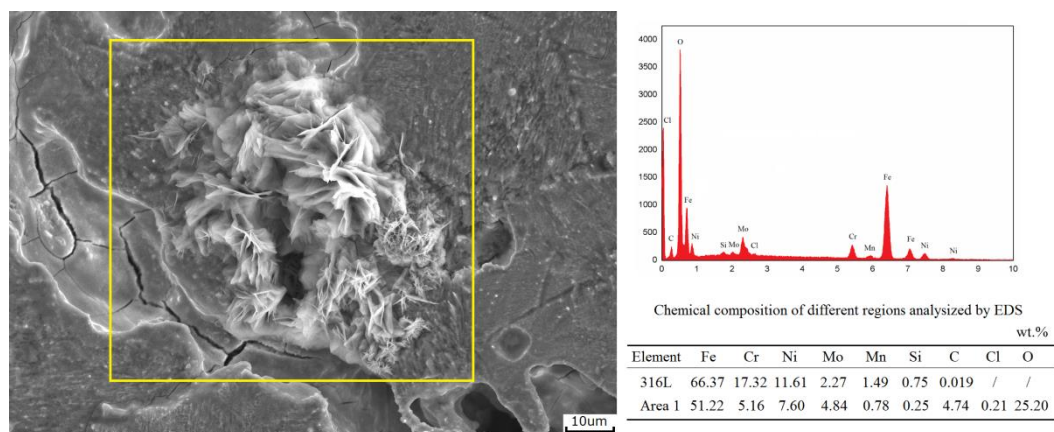
Figure 10. EDS spectra of the selected area of the corrosion product of the SS316L SLM sample from coarse powder after immersing in a 6.0 wt.% FeCl$_3$ solution at 25 °C for 25 days.

Additionally, the EDS measurement was used to further analyse the corrosion products of the SS316L SLM sample immersed in the 6.0 wt.% FeCl$_3$ solution at 25 °C for 25 days [33]. In the EDS spectra of Figure 10, it is evident that the corrosion products were mainly composed of Fe and O [36]. The content of Fe and O in the corrosion product was approximately 51 wt.% and 25 wt.%. Compared

with the content of Mn (2.27 wt.%) in the original SS316L SLM sample, the content of Mn (4.84 wt.%) on the surface of the corroded sample was significantly increased, which further indicated that the element of Mn was more easily corroded to form corrosion products and was enriched on the surface of the sample. There was a little Cl on the surface of the sample, mainly because most of the chloride was dissolved into the solution [37]. The presence of element Cl explained the process of Cl⁻ penetration into the matrix through the oxide film.

As shown in Figure 11, the corrosion product phases from the SS316L SLM sample immersed in a 6.0 wt.% $FeCl_3$ solution at 25 °C for 25 days were identified by X-ray diffraction pattern analyses [38]. Various phases such as iron chloride hydrate [$FeCl_2 \bullet (H_2O)_4$], chromium oxide [Cr_2O_3] and [CrO_2], nickel iron oxide [$NiFe_2O_4$], nickel chromium oxide [$NiCrO_4$], manganese oxide [Mn_2O_3], and molybdite [MoO_3] phases were detected in the XRD patterns. The XRD pattern of the corrosion products that occurred after 25 days in the 6.0 wt.% $FeCl_3$ solution illustrated that the $FeCl_2 \bullet (H_2O)_4$ phase was the major corrosion product with smaller quantities of other oxides.
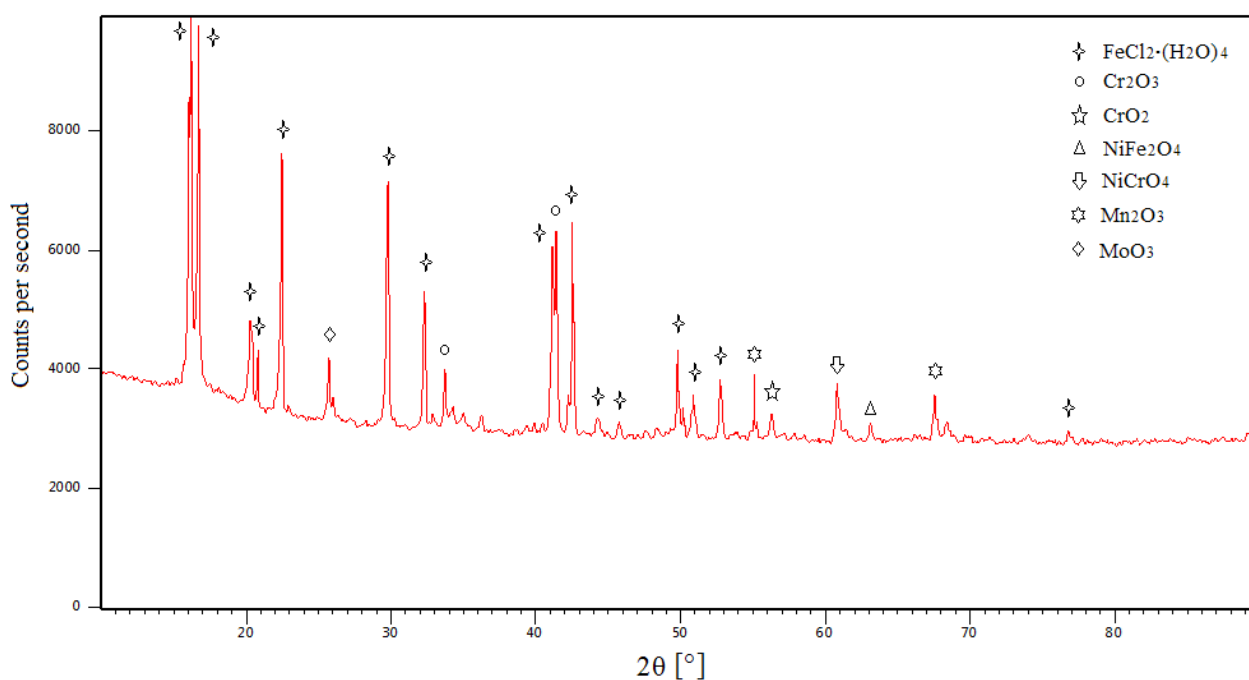
Figure 11. XRD patterns of the corrosion products of the SS316L SLM sample after immersing in a 6.0 wt.% $FeCl_3$ solution at 25 °C for 25 days.

3.3. Corrosion mechanism

Figure 12 interprets the corrosion mechanisms of SS316L produced via SLM from different size powders in the 6.0 wt.% $FeCl_3$ solution during the four stages [17]. In the first instance, a stable passive layer was generated on the surface of the sample, pores, cracks and un-melted powders (Figure 12b).

During Stage 2, for the smooth and rough surfaces, Cl⁻ entered into the matrix in different ways. For a smooth surface, the Cl⁻ with small ion radius in the 6.0 wt.% $FeCl_3$ solution began to

attack and break through passivation membrane into the internal matrix to form pitting corrosion. For the rough surface (containing cracks, pores and un-melted powder), the Cl^- first entered into the cracks and pores to facilitate crevice corrosion because of the high surface free energy of the cracks and pores [19]. Meanwhile, due to the strong oxidation of Fe^{3+} in the solution, Fe was oxidized to Fe^{2+}, Cr was oxidized to Cr^{3+} and Cr^{4+}, Ni was oxidized to Ni^{2+}, Mn as oxidized to Mn^{3+} and Mo was oxidized to Mo^{6+}. In this study, Fe, Cr, Ni, Mn and Mo acted as the anodes. The reaction mechanism was shown in equations (1) - (5). The cathodic reaction must balance the dissolution reaction of the SS316L SLM sample substrate in the anode. The reduction of Fe^{3+} is the most dominant cathodic reaction that occurred, as shown in equation (6) [39].

$$Fe \rightarrow Fe^{2+} + 2e \quad (1)$$
$$Cr \rightarrow Cr^{2+} + 2e \quad (2)$$
$$Ni \rightarrow Ni^{2+} + 2e \quad (3)$$
$$Mn \rightarrow Mn^{3+} + 3e \quad (4)$$
$$Mo \rightarrow Mo^{6+} + 6e \quad (5)$$
$$Fe^{3+} + e \rightarrow Fe^{2+} \quad (6)$$
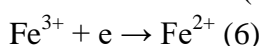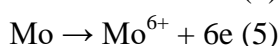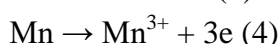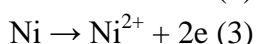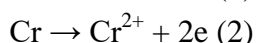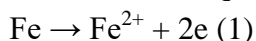
During Stage 3, as shown in Figure 12d, the corrosion products accumulated on the substrate surface, and the most of the corrosion products on the smooth surface fell off into the $FeCl_3$ solution, so that the matrix was again exposed to the corrosion solution, repeating the process of Stage 2. The corrosion products on the rough surface were mostly enriched on the surface, and the vast majority of the corrosion products in the cracks were deposited and blocked the corrosion channels to prevent further corrosion.

In the end, the general disintegration of the corrosion products could be observed (Figure 12e).
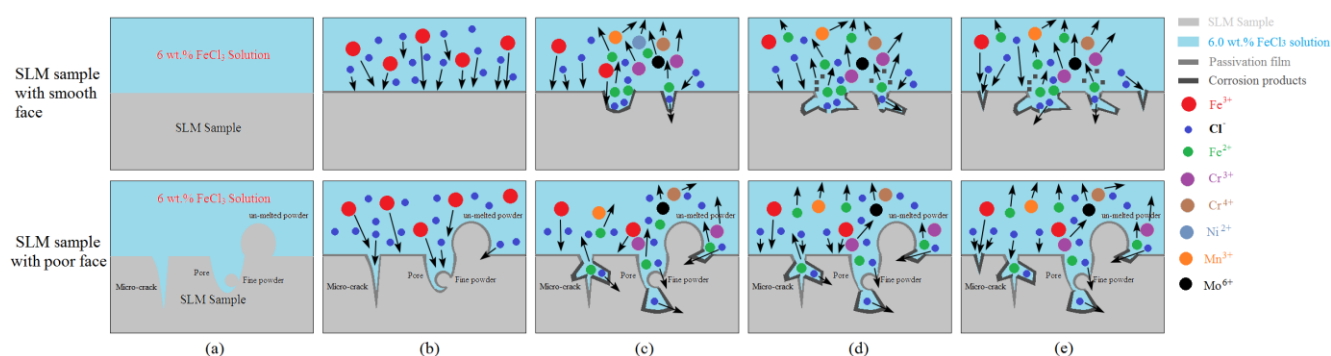
Figure 12. Corrosion mechanisms of SS316L produced via SLM, stage 0: Initial stage (a), stage 1: passive layer is generated on the surface of the sample (b), stage 2: attack and breakage through the passivation membrane (c), stage 3: corrosion products fall off or are deposited on the surface (d), stage 4: further attack and breakage through the passivation membrane (e).

In summary, these processes could explain the higher corrosion rates of the SS316L SLM samples in a 6.0 wt.% $FeCl_3$ solution.

4. CONCLUSION

The microstructure, defects and corrosion characteristics of three SS316L SLM samples produced from three types of powder with different particle size distributions in a 6.0 wt.% $FeCl_3$ solution were investigated. The following conclusions were drawn.

(1) SLM samples from the fine powder exhibited the best surface quality, which was smoother with less porosity and un-melted powder, while the SLM samples from coarse powder and raw powder possessed more pores and un-melted powders under the same SLM processing parameters.

(2) From the electrochemical polarization curves, the SLM sample from fine powder showed the lowest corrosion tendency, and the corrosion characteristics of the SLM sample from coarse powder was similar to that of the SLM sample from raw powder. The i_{corr} and weight loss showed that the corrosion rate of the fine powder sample was the fastest.

(3) For the SS316L SLM sample, the Mn element was easily corroded and formed a corrosion product layer that acted like a barrier, while the Mo and Ni elements were more easily protected in the 6.0 wt.% $FeCl_3$ solution.

References

1. H. Zhong, X. Yao, Y. Zhu, J. Zhang, D. Jiang, J. Chen, Z. Chen, X. Liu and Z. Huang, *J. Ceram. Sci. Tech.,* 06 (2015) 133.
2. J.S. Park; M.G. Lee, Y.J. Cho, J.H. Sung, M.S. Jeong, S.K. Lee, Y.J. Choi and D.H. Kim, *Met. Mater. Int.,* 22 (2016) 143.
3. Y. Zou, Q. Han, X.S. Weng, Y.W. Zou, Y.Y. Yang, K.S. Zhang, K.R. Yang, X.L. Xu, C.Y. Wang, Y.G. Qin and J.C. Wang, *Medicine,* 6 (2018) 97.
4. K.A. Ibrahim, B. Wu and N.P. Brandon, *Mater. Design,* 106 (2016) 51.
5. Z.J. Sun, X.P. Tan, S.B. Tor, W.Y. Yeong, *Mater. Design,* 104 (2016) 197.
6. A. Hinojos, J. Mireles, A. Reichardt, P. Frigola, P. Hosemann, L.E. Murr and R.B. Wicker, *Mater. Design,* 94 (2016) 17.
7. R.K. Enneti, K.C. Prough, T.A. Wolfe, A. Klein, N. Studley and J.L. Trasorras, *Int. J. Refract. Met. H.,* 71 (2018) 28.
8. Y. Zhong, L.F. Liu, S. Wikman, D.Q. Cui and Z.J. Shen, *J. Nucl. Mater.*, 470 (2016) 170.
9. K.V. Yang, Y.J. Shi, F. Palm, X.H. Wu and P. Rometsch, *Scripta Mater.*, 145 (2018) 113.
10. K. Kunze, T. Etter, J. Grässlin and V. Shklover, *Mater. Sci. Eng. A*, 620 (2015) 213.
11. L.B. Zhou, T.C. Yuan, R.D. Li, J.Z. Tang, G.H. Wang and K.X. Guo, *Mater. Sci. Eng. A*, 707 (2017) 443.
12. S. Leuders, M. Thöne, A. Riemer, T. Niendorf, T. Tröster, H.A. Richard and H.J. Maier, *Int. J. Fatigue*, 48 (2013) 300.
13. Z.L. Lu, A.F. Zhang and Z.Q. Tong, *Mater. Manuf. Process.*, 26 (2011) 879.
14. D.K. Pattanayak, A. Fukuda and T. Matsushita, *Acta Biomater.*, 7 (2011) 1398.
15. Y. Sun, A. Moroz and K. Alrbaey, *J. Mater. Eng. Perform.,* 23 (2014) 518.
16. Y.Z. Zhang, F.R. Liu, J.M. Chen and Y.P. Yuan, *J. Laser Appl.*, 29 (2017) 022306.
17. K. Geenen, A. Röttger and W. Theisen, *Mater. Corros.*, 68 (2017) 764.

18. E. Otero, A.A Pardo, M. V. Utrilla, E. Sáenz and J.F. Álvarez, *Corros. Sci*, 40 (1998) 1421.
19. D. Itzhak and E. Aghion, *Corros. Sci.,* 23 (1983) 1085.
20. P. Nandwana, A.M. Elliott, D. Siddel, A. Merriman, W.H. Peter and S.S. Babu, *Curr. Opin. Solid St. M.*, 21 (2017) 207.
21. P.P. Ding, A.Q. Mao, X. Zhang, X. Jin, B. Wang, M. Liu and X.L. Gu, *J. Alloy. Compd.,* 721 (2017) 609.
22. A.Y. Chen, W.F. Hu, D. Wang, Y.K. Zhu, P. Wang, J.H. Yang, X.Y. Wang, J.F. Gu and J. Lu, *Scripta Mater.,* 130 (2017) 264.
23. L.Y. Chen, J.C. Huang, C.H. Lin, C.T. Pan, S.Y. Chen, T.L. Yang, D.Y. Lin, H.K. Lin and J.S.C. Jang, *Mater. Sci. Eng. A*, 682 (2017) 389.
24. N.J. Harrison, I. Todd and K. Mumtaz, *J. Mater. Sci.*, 52 (2017) 10517.
25. K. Sasaki and G.T. Burstein, *Corros. Sci.,* 38 (1996) 2111.
26. G. Sander S. Thomas, V. Cruz, M. Jurg, N. Birbilis, X. Gao, M. Brameld and C.R. Hutchinson, *J. Electrochem. Soc.*, 164 (2017) 250.
27. E. Mccafferty, *Corros. Sci.,* 45 (2003) 1421.
28. J. Soltis, *Corros. Sci.,* 90 (2015) 5.
29. A.B. Radwan, A.M. Abdullah, H.J. Roven, A.M. Mohamed and M.H. SK, *Int. J. Electrochem. Sci.,* 10 (2015) 7606.
30. Q. Chao, V. Cruz, S. Thomas, N. Birbilis, P. Collins, A. Taylor, P.D. Hodgson and D. Fabijanic, *Scripta Mater.*, 141 (2017) 94.
31. M. Bojinov, G. Fabricus, T. Laitinen, K. Mäkelä, T. Saario, G. Sundholm, *Electrochim. Acta*, 46 (2001) 1339.
32. W.Y. Lai, W.Z. Zhao, Z.F. Yin and J. Zhang, *Surf. Interface Anal.*, 44 (2012) 505.
33. Y. Chen, J.X. Zhang, X.H. Gu, N.W. Dai, P. Qin and L.C. Zhang, *J. Alloy. Compd.,* 747 (2018) 648.
34. M. Cabrini, S. Lorenzi, T. Pastore, S. Pellegrini, E.P. Ambrosio, F. Calignano, D. Manfredi, M. Pavese and P. Fino, *Electrochim. Acta*, 206 (2016) 346.
35. K. Jung, H.J. Heo, J.H. Lee, Y.C. Park and C.Y. Kang, *Corros. Sci.*, 98 (2015) 748.
36. M. Qin, W.C. Xu, L.H. Yang and Y.T. Li, *Int. J. Electrochem. Sci.,* 13 (2018) 6537.
37. K.E. García, A.L. Morales, C.A. Barrero and J.M. Greneche, *Corros. Sci.,* 48 (2006) 2813.
38. Y. Behnamian, A. Mostafaei, A. Kohandehghan, B. Zahiri, W.Y. Zheng, D. Guzonas, M. Chmielus, W.X. Chen and J.L. Luo, *J. Supercrit. Fluid.,* 127 (2017) 191.
39. W.S.W. Harun, R.I.M. Asri, F.R.M. Romlay, S. Sharif, N.H.M. Jan and F. Tsumori, *J. Alloy. Compd.,* 748 (2018) 1044.